Modeling of very low frequency motions during RIPEX

A. J. H. M. Reniers,[1,2] J. H. MacMahan,[3] E. B. Thornton,[3] and T. P. Stanton[3]

[1] Numerical computations are used to explain the presence of very low frequency motions (VLFs), with frequencies less than 0.004 Hz, in the rip current velocity signals observed during the Rip-current field Experiment (RIPEX) field experiment. Observations show that the VLF motions are most intense within the surfzone and then quickly taper off in the offshore direction. By comparing computed VLF intensity ($U_{RMS,vlf}$) distributions in both the cross-shore and alongshore direction with observations in a qualitative sense, the most important contributions to the VLF dynamics are established. VLF motions at neighboring rip-channels are seen to interact in the computations, with stronger surfzone intensity for increasing bathymetric variation. The intermittent forcing by spatially varying wave groups is essential in obtaining the correct $U_{RMS,vlf}$ distribution in the cross-shore direction, suggesting this is the predominant mechanism responsible for the generation of the VLF motions observed during RIPEX. Computations also suggest that VLF motions can occasionally propagate offshore but are mostly confined to the surfzone corresponding to surfzone eddies. A quantitative comparison shows good correspondence between model computations and measurements of $U_{RMS,vlf}$ with a model skill of $O(0.7)$, with generally increased (decreased) $U_{RMS,vlf}$ during mean low (high) water levels.

1. Introduction

[2] Low-frequency gravity-driven oscillations in rip-channel flows have been observed [*Sonu*, 1972; *Aagaard et al.*, 1997; *Brander and Short*, 2001] and are typically thought to be related to changes in mass flux associated with incident wave groups [*Munk*, 1949] or infragravity waves generated by the wave groups [*Sonu*, 1972; *MacMahan et al.*, 2004a]. More recently, very low frequency vorticity motions (VLFs) in rip-current flows have been observed both in the field [*Smith and Largier*, 1995; *MacMahan et al.*, 2004b] and in laboratory conditions [*Haller and Dalrymple*, 2001]. *Smith and Largier* [1995] suggested the VLFs could be due to the shear instability of the longshore current, whereas *Haller and Dalrymple* [2001] considered the shear instability of the rip current itself. *MacMahan et al.* [2004b] hypothesize that the VLFs are surfzone eddies generated by wave groups. In reality, all contributions are potentially present, with grouped short waves incident on a rip-channeled beach generating infragravity waves and surfzone eddies with coexisting instabilities generated by the velocity shear of the mean alongshore and cross-shore

flows. The vorticity motions in the rip current are expected to manifest themselves outside the gravity-restoring region, defined by zero-mode edge wave dispersion curves, at significantly lower frequencies ($f < 0.004$ Hz) than the infragravity waves (0.004 Hz $< f <$ 0.04 Hz), based on both observations [*MacMahan et al.*, 2004a, 2004b] and theoretical considerations taking into account the velocity shear of the rip current [*Haller and Dalrymple*, 2001]. Given the fact that VLF motions are vortical with little surface expression compared with the low-frequency (LF) surface gravity waves, a separate treatment is warranted for VLF motions, which is presented here.

[3] Modeling of VLFs in rip-channel flows has been limited to synthetic geometries both for numerical [*Yu and Slinn*, 2003] and laboratory simulations [*Chen et al.*, 1999; *Haller and Dalrymple*, 2001; *Haas et al.*, 2003] and have ignored the contributions of the randomness of the incident waves on the generation of VLF motions. *Yu and Slinn* [2003] observed the generation of rip-current instabilities in their computations, where the instabilities originated within the rip current (without wave-current interaction) or in the feeder channels (with wave-current interaction). *Haas et al.* [2003] compared their numerical computations with the experimental data obtained by *Haller and Dalrymple* [2001] and concluded that inclusion of mixing associated with the vertical structure of the flow [*Putrevu and Svendsen*, 1999] reduced the computed instability intensities significantly. *Haller and Dalrymple* [2001] used a linear stability analysis to predict the temporal and spatial scales of the rip-

---

[1]Department of Civil Engineering and Geosciences, Delft University of Technology, Delft, Netherlands.
[2]Division of Applied Marine Physics, Rosenstiel School of Marine and Atmospheric Science, University of Miami, Miami, Florida, USA.
[3]Oceanography Department, Naval Postgraduate School, Monterey, California, USA.

current instabilities observed during their experiment and obtained good agreement.

[4] Here model computations are compared with measurements of VLF motions obtained during the Rip-current field Experiment (RIPEX). RIPEX provides the first comprehensive data set of rip-current VLFs under field conditions with varying forcing conditions throughout a large number of tidal cycles. This enables an examination of the effects of wave height variations and tidal elevation on the generation of rip-current VLFs utilizing a nonlinear flow model. The numerical model describes the propagation of wave group energy made up of the directionally spread incident sea/swell waves over a variable bathymetry. The wave group energy is transferred to a roller prior to dissipation to simulate breaking processes. The wave group varying wave and roller energies are used to construct the radiation stress tensors and their divergences to drive mean, infragravity, and VLF motions. The model description is given by *Reniers et al.* [2004a], who assessed the role of stochastic wave group forcing in the generation of rip channels on an initially alongshore uniform embayed beach. Comparisons of model computations with observations of infragravity waves observed during RIPEX showed good correspondence throughout the experiment [*Reniers et al.*, 2006].

[5] Model computations are carried out with constant parameter values for roller dissipation and wave breaking, where the appropriate values have been determined from previous calculations considering the modeling of infragravity conditions [*Reniers et al.*, 2006]. All computations presented here are performed with wave-current interaction on the wave group timescale. The constant model constituents of turbulent eddy viscosity and bottom friction in combination with wave-current interaction were determined quantitatively by examining the model skill, on the basis of comparisons of simulated and observed cross-shore and alongshore velocity intensity of the VLFs and mean flow strength resulting in a manning number of 0.015 for the friction formulation. Computations are performed to establish the potentially important forcing mechanisms of VLF motions by considering monochromatic, bichromatic, and random waves of equal mean energy incident on a rip-channeled beach for different rip-channel configurations.

2. RIPEX VLF Measurements

[6] The measurements were obtained during RIPEX in concert with the Steep Beach Experiment (SBE) at Sand City, Monterey Bay, California, USA. The bathymetry during the experiment consisted of shore-connected shoals intersected by relatively narrow rip channels at approximately 125 m alongshore intervals (left panel of Figure 1). Although significant changes occurred within the nearshore bathymetry, the larger morphological features stayed more or less in place. For details on the morphodynamics during the experiment, refer to the sutdy by *MacMahan et al.* [2005].

[7] The instrument setup consisted of a cross-shore array over the shoal and an alongshore array coinciding with the beginning of the rip channels (left panel of Figure 1). An example of the measured low-pass filtered ($f < 0.04$ Hz) current velocities obtained at Puv11 (right upper and middle panel of Figure 1), located in a feeder/rip channel, displays infragravity motions and slow oscillations at the VLF

timescale (250 s and longer). There is no clear evidence in the surface elevation for the presence of these VLF oscillations, similar to the observations by *Oltman-Shay et al.* [1989] for the shear instabilities in the longshore current, suggesting that these motions are not associated with surface gravity waves. *MacMahan et al.* [2004b] show that these oscillations are indeed vorticity-induced oscillations.

[8] The intensity of the VLF motions is defined by the root mean square (RMS) VLF speed, $U_{RMS,vlf}$:

$$U_{RMS,vlf} = \sqrt{\int_{\delta f}^{0.004\,\text{Hz}} S_{uu}(f) + S_{vv}(f)\,df} \quad (1)$$

where the frequency resolution, δf, equals 0.00014 Hz on the basis of a 2-hour time series, and $S_{uu}(f)$ and $S_{vv}(f)$ represent the variance density spectra of the cross-shore and alongshore velocities. This definition holds for both measurements and model computations.

[9] In general, the observed cross-shore distribution of $U_{RMS,vlf}$ has a maximum within the surfzone and then quickly tapers off in the seaward direction (upper panel of Figure 2). The corresponding alongshore distribution of $U_{RMS,vlf}$ (lower panel of Figure 2) measured at the alongshore array shows that VLFs are present both on the shoal and within the rip channel with an elevated intensity in the proximity of the rip channel. These distributions show that the VLFs are mostly contained within the surfzone, and thus the offshore propagation of vortices generated within the surfzone is limited. The observed cross-shore and alongshore distributions are used to determine which mechanisms are the most likely to contribute to the generation of VLFs.

3. Generation of VLFs

[10] Potential generation mechanisms are shear instabilities in the strongly sheared rip-current flows [*Haller and Dalrymple*, 2001; *Yu and Slinn*, 2003], the forcing of slowly modulating rip-current velocities by regular wave groups made up of two intersecting wave trains [*Fowler and Dalrymple*, 1990], the quasi-steady circulations induced by individual obliquely incident wave groups considered by *Ryrie* [1983], or a sequence of random wave groups made up of a directionally spread incident wavefield considered by *Reniers et al.* [2004a].

[11] The following considerations include monochromatic waves (no groups), bichromatic waves (regular groups), and directionally spread random waves (stochastic groups). The processes investigated that are potentially important in the VLF response are rip-channel configuration and eddy dynamics [*Peregrine*, 1998; *Buhler and Jacobson*, 2001; *Reniers et al.*, 2004a]. The various processes are assessed with a numerical model to establish the dominant contributions to the VLF response observed during the RIPEX experiment.

[12] Wave-current interaction is known to affect the generation and behavior of rip-current instabilities [*Yu and Slinn*, 2003; *Haas et al.*, 2003]. To account for the presence of a current, the wave-energy balance used by *Reniers et al.* [2004a] is replaced with the wave action balance:

$$\frac{\partial N}{\partial t} + \frac{\partial N\left(c_g \cos(\theta) + U\right)}{\partial x} + \frac{\partial N\left(c_g \sin(\theta) + V\right)}{\partial y} = -\frac{D}{\sigma}, \quad (2)$$
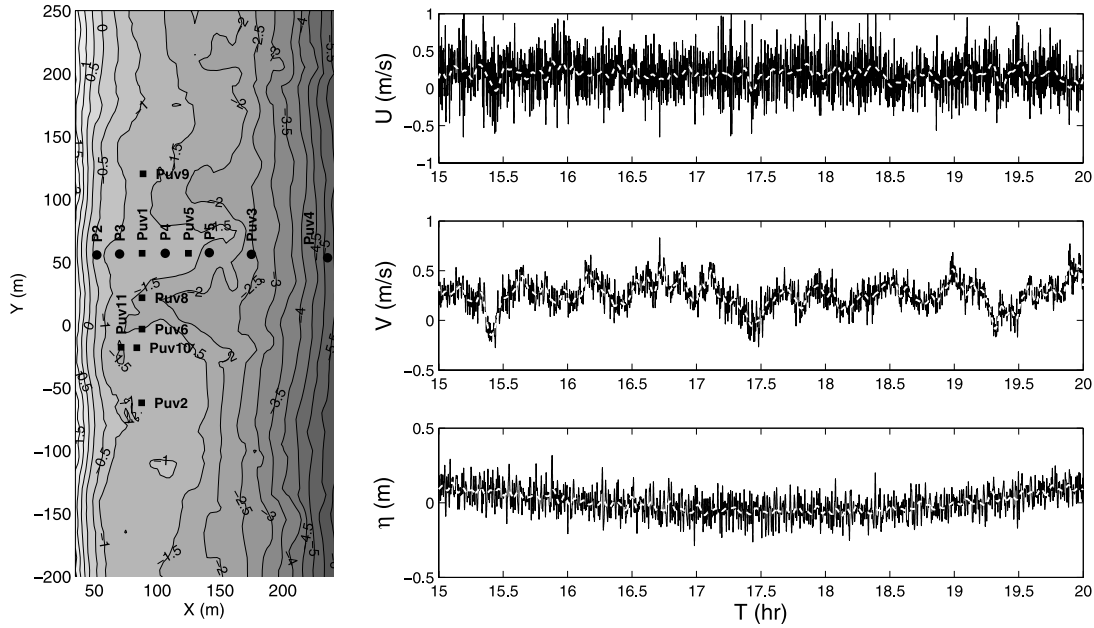
Figure 1. Left panel, survey for yearday 131 with instrument locations denoted by squares (collocated pressure and current meters denoted by Puv) and dots (pressure meters only denoted by P). Right panel, example of measured time series (thin solid lines) of low-pass filtered ($f < 0.04$ Hz) cross-shore velocity (upper plate), alongshore velocity (middle plate), and surface elevation (lower plate), showing the presence of infragravity motions superimposed on VLF motions (thick dashed white line) for Puv11.

where N represents the wave action, D is the dissipation of wave energy due to breaking modeled with the dissipation formulation of *Roelvink* [1993], and x,y are the cross-shore (positive onshore) and alongshore coordinates following the Cartesian convention. In the same manner as *Reniers et al.* [2004a], the mean direction with respect to the x axis, θ, and mean group velocity, c_g, are precomputed with the Hindcast Shallow Water Waves (HISWA) model [*Holthuijsen et al.*, 1989], taking into account the effects of directional spreading. Next these quantities are corrected for the presence of a current that varies on the timescale of the wave groups. The cross- and alongshore wave numbers, k_x and k_y, are defined as:

$$k_x = k_{x,0} + \tilde{k}_x, \tag{3}$$

$$k_y = k_{y,0} + \tilde{k}_y, \tag{4}$$

where the subscript 0 represents the wave number obtained from the precomputed refraction, and $\tilde{k}_x$ and $\tilde{k}_y$ represent the corrections associated with the presence of a time-varying current. A second set of equations is used to determine these corrections [*Witham*, 1974; *Mei*, 1985]:

$$\frac{\partial \tilde{k}_x}{\partial t} + \frac{\partial \omega}{\partial x} = 0, \tag{5}$$

$$\frac{\partial \tilde{k}_x}{\partial y} - \frac{\partial \tilde{k}_y}{\partial x} = 0, \tag{6}$$

where the absolute angular frequency, ω, is given by:

$$\omega = k_x u + k_y v + \sigma, \tag{7}$$

with u, v the cross-shore and alongshore velocities on the wave group scale, and the intrinsic angular frequency, σ, is obtained from the linear dispersion relation:

$$\sigma = \sqrt{gk\tanh(kh)} \tag{8}$$

where:

$$k = \sqrt{(k_x)^2 + (k_y)^2}. \tag{9}$$

[13] The wave group velocity c_g, utilized in the wave action balance, equation (2), is calculated from the intrinsic dispersion relation [equation (8)]:

$$c_g = \frac{\partial \sigma}{\partial k} = \left(\frac{1}{2} + \frac{kh}{\sin h(2kh)} \right) c \tag{10}$$

with c the phase speed of the waves:

$$c = \frac{\sigma}{k} \tag{11}$$

and the wave angle θ, utilized in the wave action balance, equation (2), is obtained from the cross-shore and alongshore wave number components:

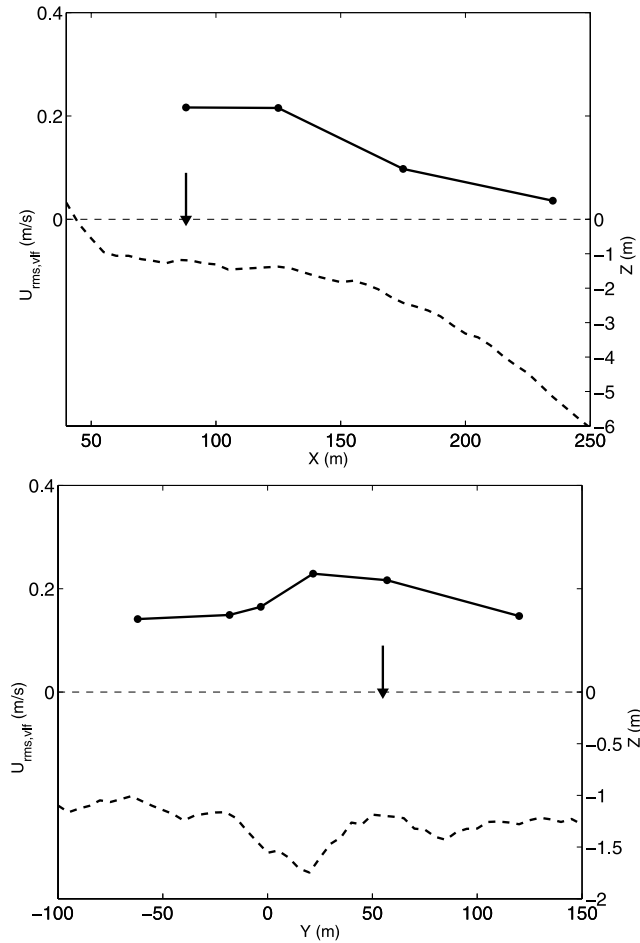$$\theta = a\tan\left(\frac{k_y}{k_x} \right). \tag{12}$$

Figure 2. Top panel, example of measured cross-shore distribution of daily averaged VLF intensity (denoted by the dots) on yearday 130. Position of alongshore array indicated by the arrow. Cross-shore bottom profile is given as a reference by the thick dashed line. Bottom panel, similar for the alongshore distribution. Position of shoal array denoted by arrow. Alongshore bottom profile is given as a reference by the thick dashed line.

[14] The equations to solve for the roller energy, radiation stresses, and flow velocities are identical to the equations used by *Reniers et al.* [2004a], with the exception of the turbulent eddy viscosity ν_t, to which a calibration coefficient, α, is added:

$$\nu_t = \alpha h \left(\frac{D_r}{\rho}\right)^{\frac{1}{3}}, \qquad (13)$$

where D_r is the dissipation of roller energy and ρ is the water density. At the offshore boundary, the incoming wave action associated with the incident waves, which can vary on the wave group scale, is prescribed in combination with a Riemann condition to absorb the outgoing long waves.

[15] The base case considers a single rip channel cutting through a shore-connected shoal (middle left panel of Figure 3). The cross-shore domain is approximately 700 m with spatially varying grid spacing (Δx) ranging from $O(15)$ m offshore to $O(4)$ m grid spacing within the surfzone. The

alongshore domain is 500 m with a constant alongshore grid spacing (Δy) of 10 m. The rip channel and shoal dimensions are similar to the RIPEX observations (compare with left panel of Figure 1). All computations cover a duration of 2 hours with a time step of 1.2 s. The turbulent mixing coefficient α is set at 0.1 on the basis of the results obtained by *Reniers et al.* [2004b] examining the vertical structure of the mean longshore and cross-shore currents obtained during the Sandy Duck field experiment. A zero normal flux condition is used at the lateral boundaries. At the shoreline, a zero normal flux is imposed at a water depth of 0.1 m. The generation and propagation of the VLF motions is examined by considering the vorticity, q:

$$q = \frac{\partial v}{\partial x} - \frac{\partial u}{\partial y}. \qquad (14)$$

4. Monochromatic Wave Forcing

[16] The first case considered is for monochromatic waves with constant height $H = 1$ m at the offshore boundary and wave period $T = 10$ s, normally incident on a coast with a single rip channel. In the presence of wave-current interaction, the incident waves shoal and refract on the outgoing rip current resulting in increased wave energy within the rip channel (upper left panel of Figure 3). This increase in wave energy is consistent with the results obtained by, e.g., *Yu and Slinn* [2003].

[17] Given the steady wave forcing, the observed VLF motions in the rip current are due to the shear instability of the rip flow [*Haller and Dalrymple*, 2001; *Yu and Slinn*, 2003]. The rip-current instabilities manifest themselves mostly outside the surf zone (middle left panel of Figure 3), defined as the area shoreward of breaking waves, occurring within approximately 180 m from the shoreline with the waves breaking generally on the outer slope of the bar. Consequently, the alongshore averaged VLF intensity, normalized with its cross-shore maximum, $U^*_{RMS,vlf}$, as a function of cross-shore distance normalized with the surf-zone width of 180 m, shows maximum VLF intensity offshore and negligible variations within the surfzone (lower left panel of Figure 3). Hence the cross-shore distribution of $U_{RMS,vlf}$ is unlike the observations that display a clear maximum within the surfzone followed by a strong decay in the offshore direction (compare with Figure 2).

[18] Next, the influence of the rip-channel configuration is examined. A first modification is the introduction of an additional rip channel with an alongshore separation length of $O(100)$ m, consistent with the RIPEX bathymetry (compare left panel of Figure 1 and right middle panel of Figure 3). The rip channel is a mirror image of the first channel located at the same cross-shore location. The presence of the second channel results in interacting VLF motions generated in both channels (middle right panel of Figure 4) causing an onset of the instabilities closer to shore compared to the case with a single rip channel (compare with left middle panel of Figure 3). As a result, the cross-shore distribution of $U^*_{RMS,vlf}$ shows an increased intensity just outside the surfzone (lower right panel of Figure 3) compared to the case with a single rip channel. Next, the second rip channel is given a small offset in the offshore direction emulating
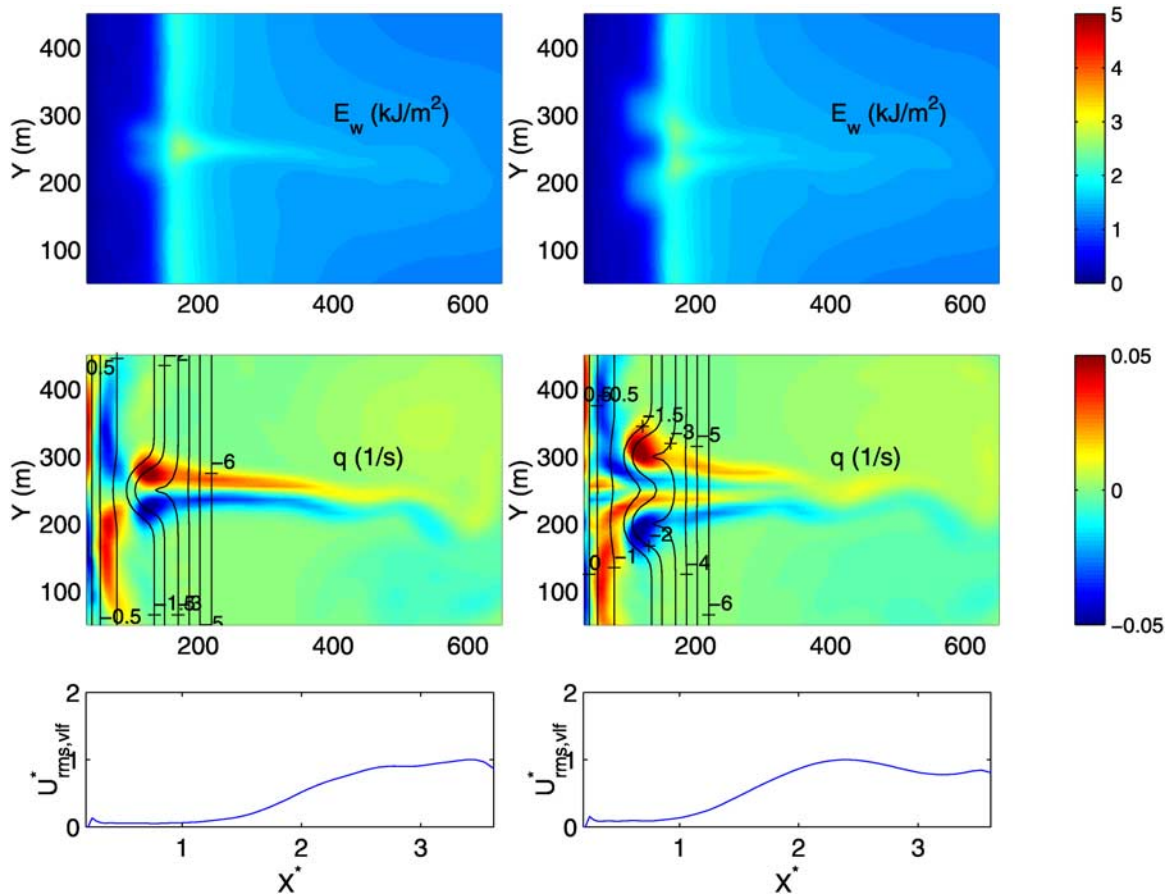
Figure 3. Left panels, snapshot of wave energy (upper panel), corresponding vorticity (middle panel), and normalized alongshore-averaged VLF intensity, $U^*_{RMS,vlf}$, as function of normalized cross-shore distance, X^*, for monochromatic waves with $H = 1$ m and $T = 10$ s, normally incident on a coast with a single rip channel, with wave-current interaction. Right panels, similar for the case of two symmetric rip channels.

the RIPEX experiment to examine the effect of asymmetry in the rip-channel configuration (left panels of Figure 4). Apparently, the asymmetry in the rip-channel configuration makes the system more conducive to the generation of VLF motions. As a result, the VLF motions are now pressed a little closer to the surfzone edge than in the case of two symmetric rip channels. Still, $U_{RMS,vlf}$ within the surfzone is significantly less than outside the surfzone, contrary to the field observations (Figure 2).

[19] As a next step, the actual measured bathymetry is used in the model computations to assess the effects of the added bathymetric variability on the VLF motions. In contrast to the previous cases, there is no longer a clear rip current present that extends well beyond the surfzone (right middle panel of Figure 4), and vorticity is mostly restricted to the surfzone. In this case, shear instabilities are generated within the surfzone; however, there is no significant offshore decay of the VLF motions, and consequently the corresponding VLF intensity within the surfzone is comparable to the offshore VLF intensity (lower right panel of Figure 4).

[20] In line with the works of *Chen at al.* [1999] and *Haas et al.* [2003], the previous results suggest that the underlying bathymetry does play an important role in the

generation of VLF motions reflected in the differences in the cross-shore distribution of the VLF intensities for different rip channel configurations. However, none of the computed cross-shore distributions match the observed distribution (Figure 2), suggesting additional mechanisms are present.

5. Bichromatic Wave Forcing

[21] For the asymmetric rip-channel configuration, different wave forcing regimes are examined. The monochromatic wave forcing (discussed above) is compared with regular wave groups made up of two incident waves of slightly different frequency and different direction, i.e., bichromatic wave forcing. This results in a spatial variation of the wave energy in both cross-shore and alongshore direction. This spatially and temporally modulated wavefield can generate alongshore periodic, slowly migrating rip currents on an alongshore uniform bathymetry as demonstrated by *Fowler and Dalrymple* [1990]. Here the effects of intersecting wave trains on the generation of VLF motions are examined on a rip-channeled beach. Two wave trains with frequencies 0.099 and 0.101 Hz, incident from different directions $\theta_1 = -1.24°$ and $40°$, with respective wave amplitudes of 0.49 and
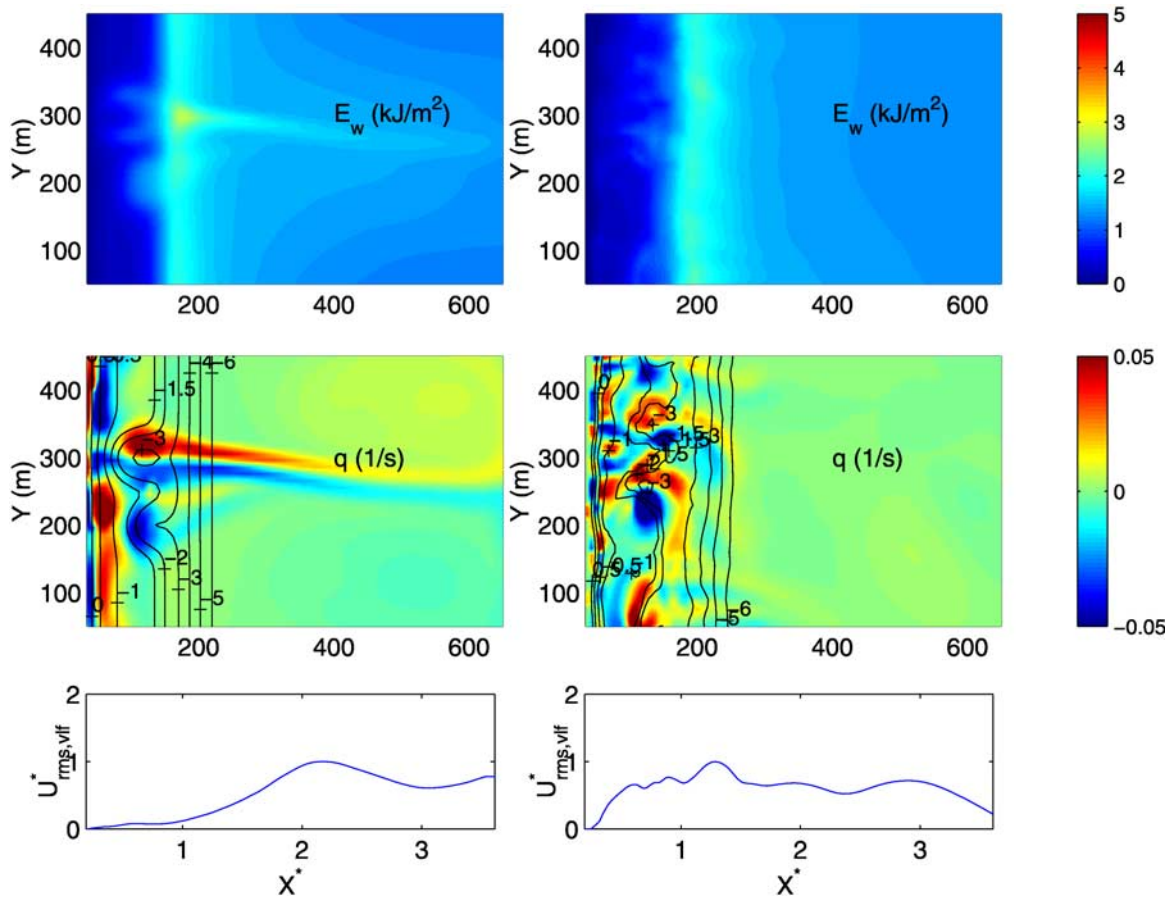
Figure 4. Left panels, snapshot of wave energy (upper panel), corresponding vorticity (middle panel), and normalized alongshore-averaged VLF intensity, $U^*_{RMS,vlf}$, as function of the normalized cross-shore distance, X^*, for regular waves with $H = 1$ m and $T = 10$ s, normally incident on a coast with two asymmetric rip channels (with an offset in the cross-shore direction). Right panels, similar for the case of the actual bathymetry.

0.10 m, generate an alongshore modulated wavefield with an alongshore spacing of 163 m (upper left panel of Figure 5) and a group period of 500 s that is within the VLF frequency range. The shear component of the radiation stress made up by the two wave trains is negligible ($\sum S_{xy} = 0$), hence there is no driving of a mean longshore current. A snapshot of the vorticity field shows strong eddy circulations within the surfzone (left middle panel of Figure 5). In addition, eddies have separated from the surfzone and are propagating offshore. The cross-shore distribution of $U^*_{RMS,vlf}$ shows a clear maximum within the surfzone at $X^* = 0.75$, decaying in the offshore direction not unlike the observations (compare lower left panel of Figure 5 with upper panel of Figure 2). The VLF intensity outside the surfzone is still overpredicted, suggesting that the offshore eddy formation is too strong. This may be related to the timescale of the forcing. If the difference frequency of the two intersecting wave trains is small, there is enough time for the rip current to develop and reach offshore. Once the wave group forcing changes, this rip current is then cut off from the surfzone, and what remains are eddy-like features travelling offshore. In contrast, the timescale of wave groups made up of directionally spread incident waves is typically much shorter, i.e., in the infragravity band. As a result, the forcing of the rip current is constantly changing, and the resulting rip-current eddies are expected to remain closer to the surfzone. This is examined next for the case of irregular wave groups.

6. Directionally Broad Stochastic Wave Forcing

[22] A stochastic description of the spatially and temporally varying wave forcing is obtained by considering random wave groups made up of directionally spread incident waves [*Reniers et al.*, 2004a]. The wave-action at the offshore boundary for a Jonswap spectrum with a RMS wave height, H_{RMS} of 1.0 m, and a peak period, T_p, of 10 s, in combination with a $\cos^s(\theta - \bar{\theta})$ − directional spreading function with $s = 20$, centered around $\bar{\theta} = 0°$ is obtained with the method outlined by *Van Dongeren et al.* [2003]. Introducing this formulation into the wave-action balance [equation (2)] results in a strikingly different picture of the spatial variation of the wave energy on the wave group scale, both in the alongshore and cross-shore directions (upper right panel of Figure 5). The wave energy has the appearance of random blobs incident on the shoreline, where upon breaking, result in radiation stress gradients. The spatial modulation of the wave energy generates both
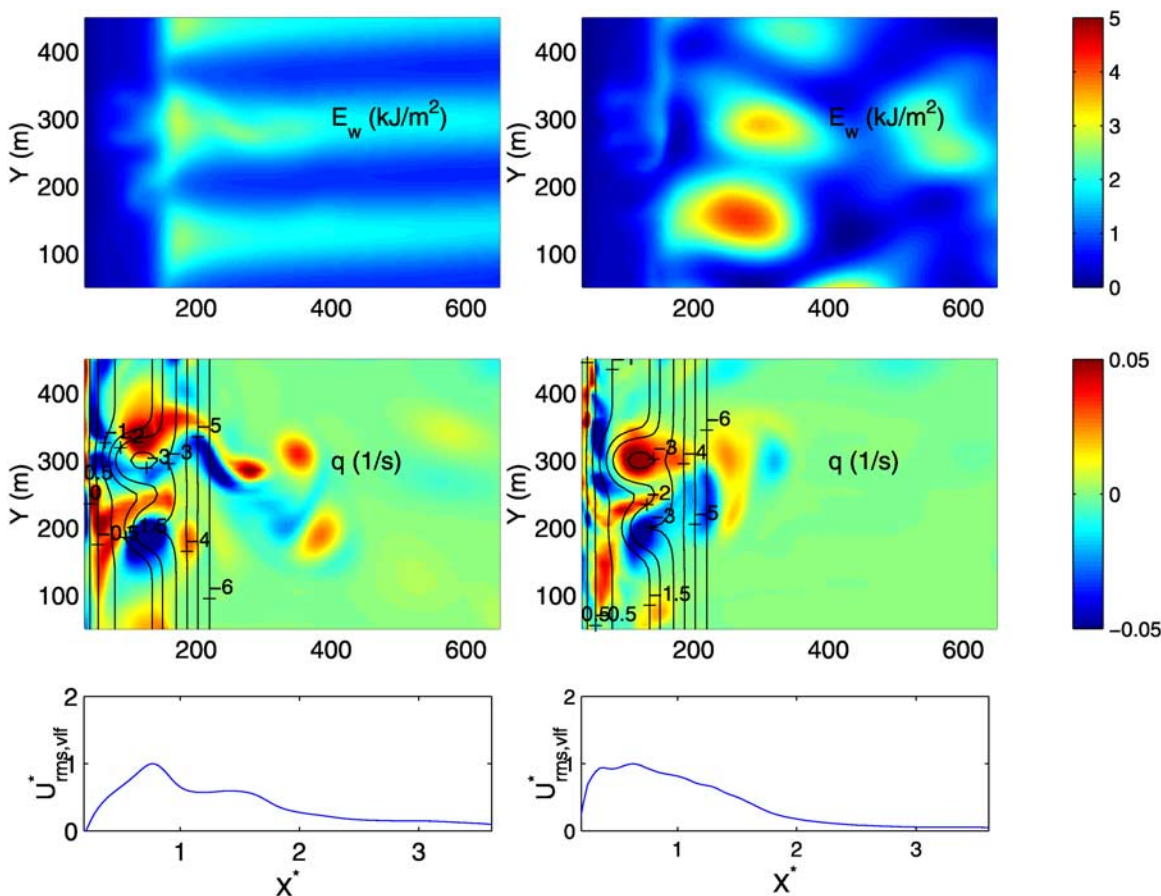
Figure 5. Left panels, snapshot of wave energy (upper panel), corresponding vorticity (middle panel), and normalized alongshore-averaged VLF intensity, $U^*_{RMS,vlf}$, as function of normalized cross-shore distance, X^*, for bichromatic wave groups made up of two intersecting waves with a mean frequency of 0.1 Hz and a frequency difference of 0.002 Hz and zero mean wave direction. Right panels, similar for wave groups made up of a directionally spread Jonswap spectrum with $H_{RMS} = 1.0$ m, $T_p = 10$ s and zero mean direction.

infragravity motions and VLF motions. The vorticity associated with the VLF motions, obtained by low-pass filtering the velocities using a cutoff frequency of 0.004 Hz, is indeed mostly confined to the surfzone (middle right panel of Figure 5). The corresponding cross-shore distribution of $U^*_{RMS,vlf}$ shows a maximum within the surfzone, which quickly drops off in the offshore direction. This drop-off occurs sooner compared to the case with bichromatic wave groups (compare lower panels of Figure 5).

[23] The fact that the modeled cross-shore distribution of $U_{RMS,vlf}$ is similar to the observations suggests that the most important processes are present in the numerical modeling. A quantitative comparison with the observations is performed in the following.

7. Comparison with Observations

[24] Wave boundary conditions for the model are obtained from the offshore directional wave rider buoy, located in 17 m water depth [*Reniers et al.*, 2006], and the tidal elevation is obtained from a National Oceanic and Atmospheric Administration/National Ocean Service wave gauge located near the Monterey harbor 2 km south of the

experiment site. Hourly estimated frequency-directional spectra are used to generate time series for the spatially and temporally varying wave action using a single summation method [*Van Dongeren et al.*, 2003]. Using the measured bathymetry, which is periodically extended in the alongshore direction to a total length of 1100 m to mitigate boundary effects, the wave and flow field on the wave group scale are computed. Time step and grid spacing are the same as for the idealized cases.

[25] The computed time series of the flow velocities and surface elevation at Puv11 for yearday 130, hours 15–20, show similar signals compared with the measurements in both the LF and VLF timescales (compare right panels of Figure 1 with Figure 6). The RMS wave height at this time is approximately 1 m with a mean wave period of 10 s and normal incidence. Note that the model is run in a stochastic mode; that is, the wave action boundary signal is constructed from the measured frequency-directional wave spectrum as opposed to utilizing the measured surface elevation time series at the offshore buoy. The computed and measured signals are therefore not expected to match in a deterministic sense but in a statistical sense.
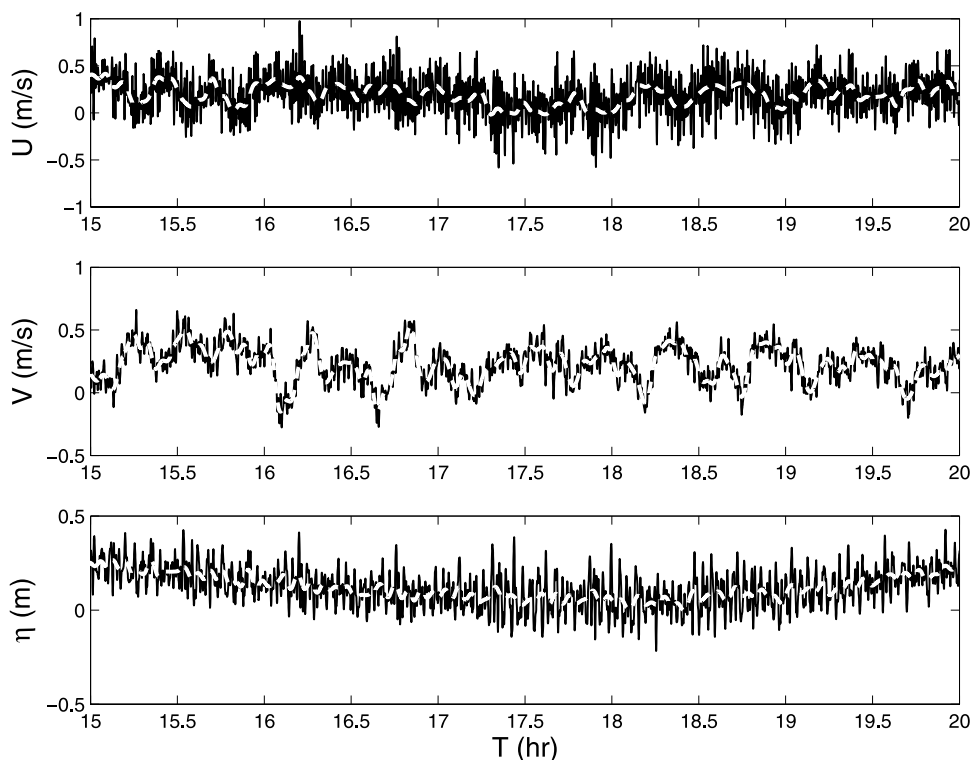
Figure 6. Example of computed time series of low-pass filtered ($f < 0.04$ Hz) cross-shore velocity (upper plate), alongshore velocity (middle plate), and surface elevation (lower plate), showing the presence of infragravity motions (thin line) superimposed on VLF motions (thick dashed white line) for yearday 130, hours 15–20.

[26] A comprehensive comparison of the model computations with the measured LF motions for the duration of the RIPEX experiment expressed in a skill factor [e.g., *Gallagher et al.*, 1998] is given by *Reniers et al.* [2006], which resulted in a model skill of 0.85 for the incident RMS wave height, $H_{RMS,hi}$, 0.81 for the RMS infragravity wave height, $H_{RMS,lo}$, and model skills of 0.76 and 0.65 for the RMS low-frequency velocity motions, $u_{RMS,lo}$ and $v_{RMS,lo}$. These results demonstrate that wave and roller energy dissipation are well calibrated. However, in addition to the wave forcing, the mean velocity field responsible for transporting the VLF motions is important and is assessed next.

[27] The computed mean flow pattern exhibits strong offshore directed flows within the rip channels reaching velocities up to 0.8 m/s (left panel of Figure 7). The northern rip channel, located at $Y = 20$ m, has a more or less closed circulation cell, where water carried offshore by the rip current returns over the relatively shallow shoal. In contrast, the southern rip channel, located at $Y = 125$ m, carries most of the excess water associated with the mass flux of the incident sea/swell waves offshore without returning. A comparison with the measured mean velocities shows reasonable correspondence (right panel of Figure 7), suggesting the mean motions are well represented by the model computations at this time.

[28] Given the fact that the offshore extent of shear instabilities is strongly affected by the underlying mean flow field, a comparison is made between measured and computed 2-hour mean velocity through the surfzone (Figure 8). The mean flow velocities within the surfzone

are significantly larger than outside the surfzone (compare results for Puv1 with Puv4 in Figure 8). In fact, only during the storm conditions on yearday 122, the offshore sensors show mean flow velocities above 0.25 m/s. This is consistent with the limited offshore extent of the VLF motions observed during RIPEX. The cross-shore deceleration of the mean velocity is well represented by the numerical results, although significant differences at individual sensors between measured and computed mean velocities can exist.

[29] The VLF motions are examined in the following starting with the cross-shore and alongshore distributions of the daily averaged $U_{RMS,vlf}$. The computed cross-shore distribution of $U_{RMS,vlf}$ for yearday 130 shows a maximum intensity within the surfzone and subsequent decay in the offshore direction, not unlike the measurements (left upper panel of Figure 9), although the surfzone VLF intensities are underpredicted. The corresponding alongshore distribution matches the observations away from the rip channel and underpredicts the intensities close to the rip channel. The overall comparison for yearday 130 is satisfactory. Similar results are obtained for yearday 122, during the peak of the storm with an offshore RMS wave height in the order of 2 m, again with a strong decay of the VLF intensity in the offshore direction (upper right panel of Figure 9). The computed VLF intensities in the alongshore direction show less variability than the measurements but are again of the right order of magnitude (lower right panel of Figure 9).

[30] To obtain a synoptic view of the VLF motions, the computed mean velocity and mean vorticity field (left panel Figure 7) are subtracted from the calculations. Next the VLF
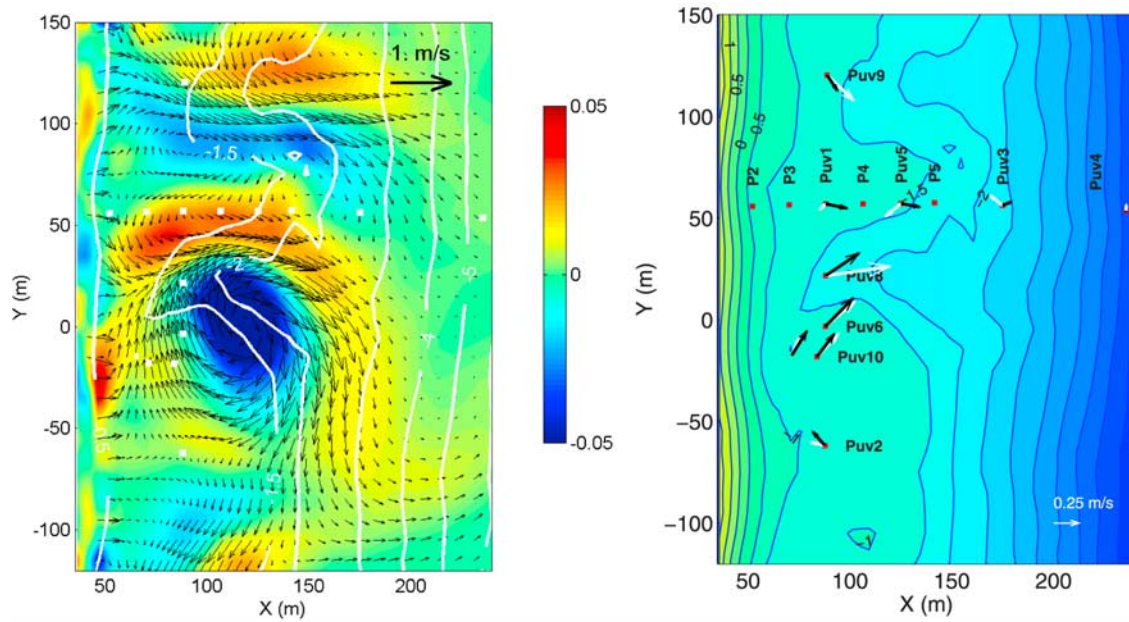
Figure 7. Left panel, computed 2-hour averaged flow velocity (see arrow for scaling) and corresponding vorticity in s^{-1} for yearday 130, hour 16. Depth contours in meters given by the solid white lines and instrument locations by the white squares. Right panel, comparison of measured mean flow velocities (white arrows) with computed mean velocities (black arrows) for yearday 130, hour 16.

velocity model computations are low-pass filtered with a frequency cutoff of 0.004 Hz eliminating most of the infragravity contributions within the velocity signal thus retaining the VLF velocity response only.

[31] Two snapshots (Figure 10), separated by a 16-min interval, of the VLF velocity field and corresponding vorticity show the presence of VLF motions in both rip channels with length scales comparable to the rip-channel
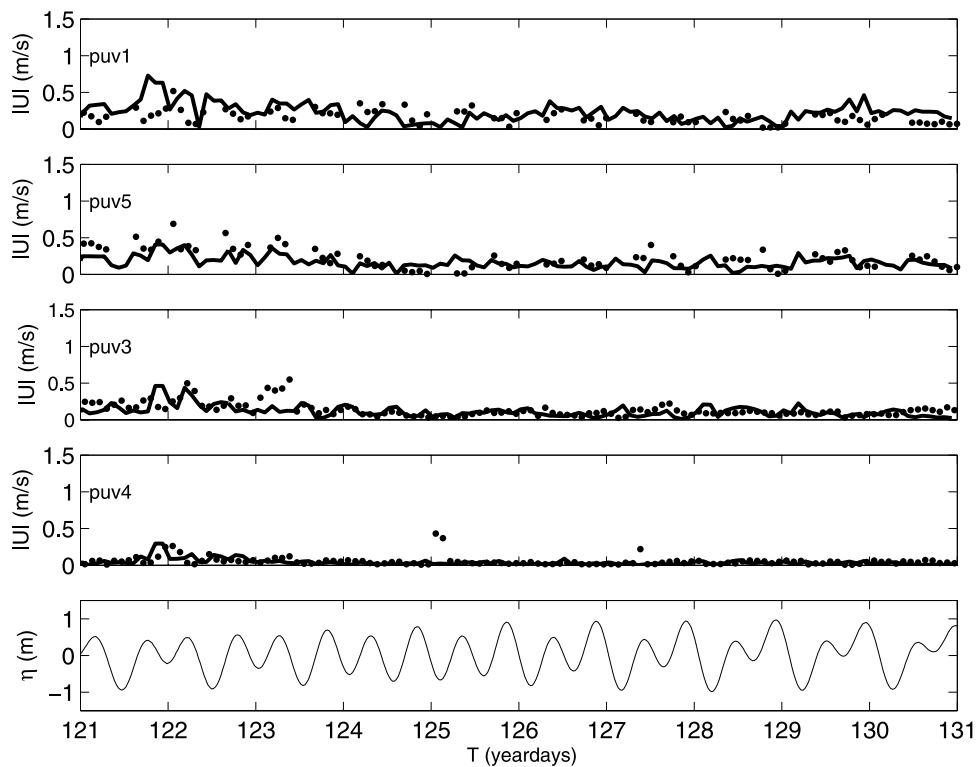
Figure 8. Computed (solid line) and measured (dots) 2-hour mean velocity magnitudes for a 10-day period at various sensors traversing the surfzone (see Figure 1 for locations). Tidal elevation is given in the lowest panel as a reference.
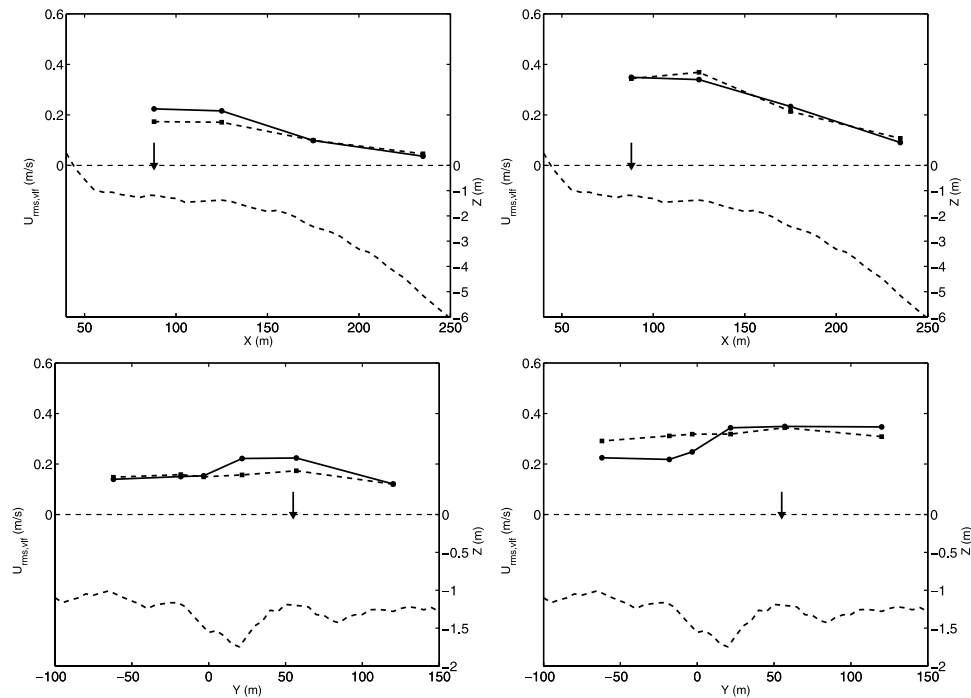
Figure 9. Left top panel, comparison of measured (dots) and computed daily averaged cross-shore VLF intensity for yearday 130 (squares). Bottom left panel, similar but for the alongshore distribution. Right top panel, comparison of measured (dots) and computed daily averaged cross-shore VLF intensity for yearday 122 (squares). Bottom right panel, similar but for the alongshore distribution.

spacing. The vorticity is concentrated along the 1.5-m depth contour, which corresponds to the location with most intense wave breaking. Closer to the shoreline, smaller pockets of vorticity can be observed. Inspection of the temporal evolution (not presented) shows that the VLF motions in the rip channel located at $Y = 20$ m are more or less trapped within the circular mean flow circulation (left panel of Figure 7). As a result, they do not propagate away from the surfzone, causing strong oscillations of the rip cell as a whole. In contrast, the VLF motions within the rip channel located around $Y = 100$ m propagate with the mean rip current in the offshore direction and occasionally
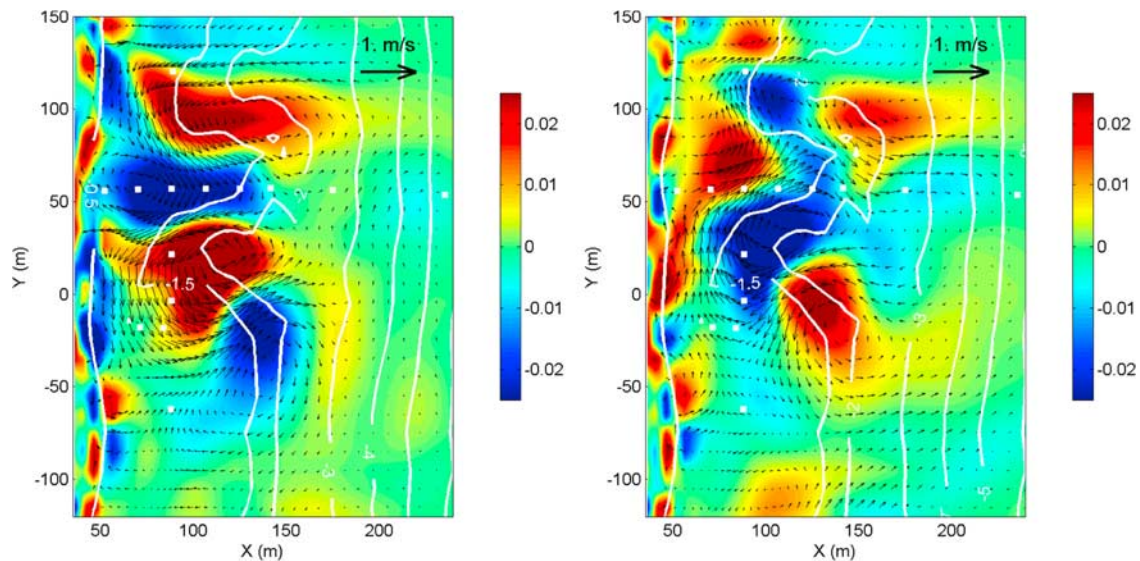

Figure 10. Snapshots of computed VLF velocity response at two separate intervals separated by 16 min showing the VLF velocity field (see arrow for scaling) and corresponding vorticity field q in s^{-1} for yearday 130, hour 16. Depth contours in meters given by the solid white lines and instrument locations by the white squares.
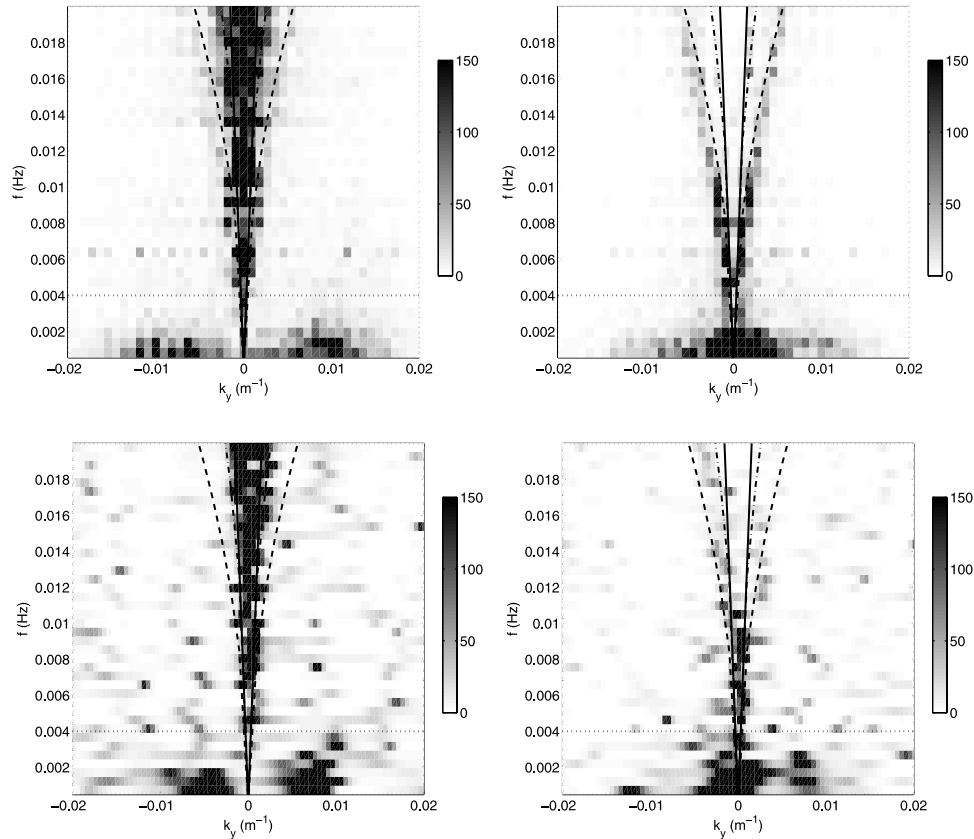
Figure 11. Upper panels, f-k_y spectra computed with two-dimensional FFT for the computed cross-shore velocity (left panel) and alongshore velocity for yearday 130, hours 16–20 at the alongshore array position ($X = 88$ m). Lower panels, f-k_y spectra computed using IMLE for the measured cross-shore velocity (left panel) and alongshore velocity for yearday 130, hours 16–20 at the alongshore array. The dashed and dash-dotted lines indicate the zero and first mode edge wave dispersion curves, and the area in between the solid lines represent the leaky wave regime. The horizontal dotted line at $f = 0.004$ Hz indicates the VLF frequency cutoff.

shoot offshore. The VLF motions are predominantly initiated at the locations of intense wave breaking, i.e., induced by groups of breaking waves along the 1.5-m depth contour. In the rip channel located around $Y = 100$ m, oscillations are sometimes initiated close to the shore and grow in intensity as they travel offshore, consistent with rip-current instabilities. Interaction between the VLFs in both channels is apparent, typically resulting in a sequence of alternating cells of positive and negative vorticity (Figure 10). These VLF circulation cells, or eddies, generally have an offset in the cross-shore direction, resulting in a wave-like pattern for the cross-shore velocity field along the alongshore measurement array, whereas the alongshore velocity field along the array is more or less homogeneous (Figure 10). As a result, the alongshore length-scales of the VLF motions are quite different for the cross-shore and alongshore velocities, which are examined next.

[32] Applying a two-dimensional fast Fourier transformation (FFT) on the computed cross-shore and alongshore velocity time series over the alongshore model domain with a duration of approximately 4 hours, subdivided into 30-min sections, results in a frequency resolution of 5.5e−4 Hz with 16 degrees of freedom. The resulting frequency wave

number, f-k_y spectra (upper panels of Figure 11) show the presence of infragravity waves, both leaky (in the cross-shore velocity, upper left panel) and trapped (along the edge-wave curves for the alongshore component, upper right panel). In the VLF frequency band, i.e., below 0.004 Hz, there is significant energy density present outside the gravity restoring region (outside the zero-mode edge wave dispersion curves) associated with VLF vorticity motions. The corresponding alongshore scale, k_y, for the cross-shore VLF motions (upper left panel) matches the rip-channel separation scale of ∼125m (left panel Figure 1). In contrast, the alongshore VLF velocity energy density is distributed around $k_y = 0$ m^{-1} (upper right panel). This difference in length scale for the VLF motions is a result of the way the surfzone eddies interact (Figure 10) as suggested by *MacMahan et al.* [2004b]. The computed VLF spectra compare well with the VLF result obtained with an iterative maximum likelihood estimator (IMLE) [*Pakwa*, 1983] utilizing the alongshore array measured velocities (lower panels of Figure 11). This holds for both cross-shore velocities (compare left panels of Figure 11) and alongshore velocities (compare right panels of Figure 11). The IMLE spectra for the computed VLF velocities (not
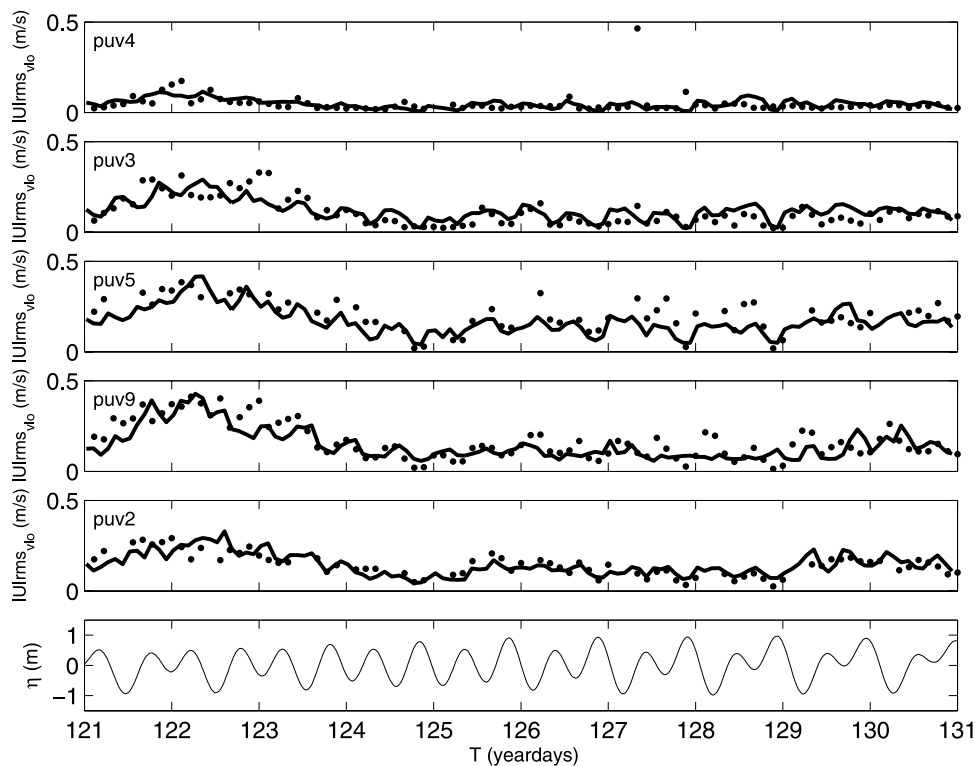
Figure 12. Comparison of measured VLF intensity (dots) with computed results for a 10-day period at various sensor locations. Tidal elevation is given in the lowest panel as a reference.

shown) yields similar results as obtained with the two-dimensional FFT, substantiating the implied assumption of spatial homogeneity of the VLF flow field when calculating the spectra.

[33] The effects of temporal changes in incident wave height and tidal elevation are examined by comparing the computed VLF intensities with the observations for a 10-day period (Figure 12). The VLF response is clearly related to the incoming wave height with increased intensities of VLF motions during storm conditions centered around yearday 122 as observed by *MacMahan et al.* [2004b]. During calmer wave conditions, the VLF response is weaker. This behavior is also present in the computations. The observed spatial variability in response (compare Puv9 with Puv2) is also present in the computed results. *MacMahan et al.* [2004b] observed a VLF response on the tidal scale (e.g., Puv9 yeardays 123 to 126, Figure 12), where $U_{RMS,vlf}$ is modulated similar to the mean currents with increased velocity at low tide. Finally, the measured offshore decay of the VLF intensities is well represented by the computations as reflected by Puv5 (within the surfzone), Puv3 (at the surfzone edge), and Puv4 (outside the surfzone) throughout the 10-day period. The average model skill for the sensors within the surfzone is 0.7 (Table 1).

8. Discussion

[34] The present numerical results for monochromatic waves (e.g., left panels of Figure 3) contrast with earlier laboratory observations of surfzone VLFs [*Haller and Dalrymple*, 2001], with strong VLF motions located within

the surfzone followed by a rapid decay in the offshore direction. The onset and the growth rate of shear instabilities in a rip-current circulation are strongly dependent on the combination of the forcing by the velocity shear and damping mechanisms such as bottom friction and turbulent eddy viscosity [*Haller and Dalrymple*, 2001]. The velocity shear within the rip channel for the laboratory conditions is an order of magnitude larger than the corresponding velocity shear during RIPEX [*MacMahan et al.*, 2006]. Hence the shear instability forcing is much stronger in the laboratory than in the RIPEX field case. This results in an onset of the instabilities within the surfzone and rapid growth of the shear instabilities while propagating with the rip current. Compared to the field case, the steeper beach slope for the laboratory conditions results in a stronger deceleration of the rip current flow, thus limiting the offshore extent of the VLF motions that are travelling with the outgoing rip

Table 1. Skill Factors for Predicted VLF Intensity at Various Sensor Locations (See Left Panel of) Within the Surfzone During Yeardays 121–130

Sensor	Skill
Puv9	0.69
Puv1	0.68
Puv6	0.66
Puv10	0.63
Puv2	0.77
Puv11	0.69
Puv5	0.72
Puv3	0.61
Mean	0.68

current. In addition, the mixing induced by the finite amplitude shear instabilities disperses the outgoing rip-current flow, thereby restricting the offshore extent of the VLF motions further. This surfzone dominance and limited offshore extent of the VLF motions was confirmed by numerical simulations [*Haas et al.*, 2003; *Chen et al.*, 1999]. In contrast, the smaller velocity shear for the RIPEX configurations presented here delays the onset of the insta-bilities to the outer surfzone, where damping associated with turbulent eddy viscosity and friction is relatively small compared to the inner surfzone where wave-breaking-in-duced turbulence (viz. equation 13) and bottom friction are important. The corresponding smaller growth rate results in persisting rip currents which take the shear instabilities offshore, well away from the surfzone.

9. Conclusions

[35] Field observations of very low frequency motions have been compared with a nonlinear shallow water model operating on the wave group timescale. The model compar-isons are made for the three different wave-forcing regimes of monochromatic waves, bichromatic waves, and broadband frequency and directional waves, all having the same H_{RMS} of 1 m, mean period of 10 s with $0°$ mean wave angle. The model constituents of turbulent eddy viscosity, bottom fric-tion in combination with wave-current interaction, were determined quantitatively on the basis of comparisons of simulated and observed cross-shore and alongshore velocity intensity of the VLFs and mean flow strength. This resulted in a single parameter set that has been used for all model computations on which the conclusions presented below are based.

[36] Model computations show that the most important contribution to explain the observed VLF motions during RIPEX is the temporal variability of the wave forcing on the group scale. For the case of monochromatic waves, only long-crested waves are incident, resulting in strong wave-current interactions; VLF motions are limited to instabilities of the rip current itself and result in the VLF energy displaced too far offshore compared with measurements. Bichromatic incident-wave energy is periodic alongshore. Strong eddy circulation occurs within the surf zone as the result of wave breaking of the wave groups. The VLF velocity intensities are confined closer to the shoreline compared with the monochromatic case.

[37] The forcing by directionally broad random waves can explain the high $U_{RMS,vlf}$ in the surf zone and the rapid decay of the intensity in the offshore direction just outside the surfzone during RIPEX. The waves are derived from the measured directional spectra offshore, which drive the waves on the wave group scale. The incident wavefield appears as "random blobs" of energy with alongshore length scales $O(200m)$, forcing VLF motions on the scale of the rip-channel spacing. The results are consistent with surf zone eddies as hypothesized by *MacMahan et al.*, 2004b. Model-predicted VLF velocity intensities forced stochastically by wave energy obtained from the measured offshore spectra are compared with measured values. The VLF velocity intensities are predicted with an average skill of 0.7.

References

Aagaard, T., B. Greenwood, and J. Nielsen (1997), Mean currents and sediment transport in a rip channel, *Mar. Geol.*, *140*, 25–45.

Brander, R. W., and A. D. Short (2001), Flow kinematics of low-energy rip current systems, *J. Coastal Res.*, *17:2*, 468–481.

Buhler, O., and T. E. Jacobson (2001), Wave-driven currents and vortex dynamics on barred beaches, *J. Fluid Mech.*, *449*, 313–339.

Chen, Q., R. A. Dalrymple, J. T. Kirby, A. B. Kennedy, and M. C. Haller (1999), Boussinesq modeling of a rip current system, *J. Geophys. Res.*, *104*, 20,617–20,637.

Fowler, R. E., and R. A. Dalrymple (1990), Wave group forced nearshore circulation, in Proceedings of the 22nd International Conference on Coastal Engineering, pp. 729–742, Am. Soc. of Civ. Eng., Delft.

Gallagher, E. L., S. Elgar, and R. T. Guza (1998), Observations of sand bar evolution on a natural beach, *J. Geophys. Res.*, *103*, 3203–3215.

Haas, K. A., I. A. Svendsen, M. C. Haller, and G. Zhao (2003), Quasi-three-dimensional modeling of rip current system, *J. Geophys. Res.*, *108*(C7), 3217, doi:10.1029/2002JC001355.

Haller, M. C., and D. A. Dalrymple (2001), Rip current instabilities, *J. Fluid Mech.*, *433*, 161–192.

Holthuijsen, L. H., N. Booij, and T. H. C. Herbers (1989), A prediction model for stationary short-crested waves in shallow water with ambient currents, *Coastal Eng.*, *13*, 23–54.

MacMahan, J., A. J. H. M. Reniers, E. B. Thornton, and T. Stanton (2004a), Infragravity rip current pulsations, *J. Geophys. Res.*, *109*, C01033, doi:10.1029/2003JC002068.

MacMahan, J. H., A. J. H. M. Reniers, E. B. Thornton, and T. P. Stanton (2004b), Surf zone eddies coupled with rip current morphology, *J. Geophys. Res.*, *109*, C07004, doi:10.1029/2003JC002083.

MacMahan, J. H., E. B. Thornton, T. P. Stanton, and A. J. H. M. Reniers (2005), RIPEX: Observations of a rip current system, *Mar. Geol.*, *218*, 113–134.

MacMahan, J. H., E. B. Thornton, and A. J. H. M. Reniers (2006), Rip current review, *Coastal Eng.*, *53*, 191–208.

Mei, C. C. (1989), *The Applied Dynamics of Ocean Surface Waves*, World Scientific, River Edge, N. J.

Munk, W. H. (1949), Surf beats, *Eos Trans. AGU*, *30*, 849–854.

Oltman-Shay, J., P. A. Howd, and W. A. Birkemeier (1989), Shear instabil-ities of mean longshore current. 2 Field observations, *J. Geophys. Res.*, *94*, 18,031–18,042.

Peregrine, D. H. (1998), Surf zone currents, *Theor. Comput. Fluid Dyn.*, *10*, 295–309.

Pakwa, S. S. (1983), Island shadows in wave directional spectra, *J. Geophys. Res.*, *88*, 2579–2591.

Putrevu, U., and I. A. Svendsen (1999), Three dimensional dispersion of momentum in wave-induced nearshore currents, *Eur. J. Mech. - B/Fluids*, *18*(3), 409–428.

Reniers, A. J. H. M., J. A. Roelvink, and E. B. Thornton (2004a), Mor-phodynamic modeling of an embayed beach under wave group forcing, *J. Geophys. Res.*, *109*, C01030, doi:10.1029/2002JC001586.

Reniers, A. J. H. M., E. B. Thornton, T. P. Stanton, and J. A. Roelvink (2004b), Vertical flow structure during Sandy Duck: Observations and modeling, *Coastal Eng.*, *51*, 237–260.

Reniers, A. J. H. M., J. MacMahan, E. B. Stanton, and T. Thornton (2006), Modeling infragravity motions on a rip-channel beach, *Coastal Eng.*, *53*, 209–222.

Roelvink, J. A. (1993), Dissipation in random wave groups incident on a beach, *Coastal Eng.*, *19*, 127–150.

Ryrie, S. C. (1983), Longshore motion due to an obliquely incident wave group, *J. Fluid Mech.*, *137*, 273–284.

Smith, J. A., and J. L. Largier (1995), Observations of nearshore circulation: Rip currents, *J. Geophys. Res.*, *100*, 10,967–10,975.

Sonu, C. J. (1972), Field observations of nearshore circulation and meandering currents, *J. Geophys. Res.*, *77*, 3232–3247.

Van Dongeren, A. R., A. J. H. M. Reniers, J. A. Battjes, and I. A. Svendsen (2003), Numerical modelling of infragravity wave response during Delilah, *J. Geophys. Res.*, *108*(C9), 3288, doi:10.1029/2002JC001332.

Witham, G. B. (1974), *Linear and Nonlinear Waves*, Wiley-Interscience, Hoboken, N. J.

Yu, J., and D. N. Slinn (2003), Effects of wave-current interaction on rip currents, *J. Geophys. Res.*, *108*(C3), 3088, doi:10.1029/2001JC001105.

————————————

J. H. MacMahan, T. P. Stanton, and E. B. Thornton, Oceanography Department, Naval Postgraduate School, Monterey, California, USA.

A. J. H. M. Reniers, Department of Civil Engineering and Geosciences, Delft University of Technology, Delft Netherlands. (a.j.h.m.reniers@tudelft.nl)